A Computationally Efficient Tool for Assessing the Depth Resolution in Potential-Field Inversion

Paoletti, V.; Hansen, Per Christian; Hansen, Mads Friis; Fedi, M.

Publication date:
2014

Document Version
Publisher's PDF, also known as Version of record

A Computationally Efficient Tool for Assessing the Depth Resolution in Potential-Field Inversion

V. Paoletti, P.C. Hansen, M.F. Hansen, and M. Fedi

Technical Report-2014-03

DTU Compute
Department of Applied Mathematics and Computer Science

A Computationally Efficient Tool for Assessing the Depth Resolution in Potential-Field Inversion[1]

V. Paoletti[1], P. C. Hansen[2], M. F. Hansen[2], and M. Fedi[1]

[1] Dipartimento di Scienze della Terra, dell'Ambiente e delle Risorse,
University Federico II, Largo S. Marcellino, 10, IT-80138 Naples, Italy
E-mail {paoletti,fedi}@unina.it

[2] Department of Applied Mathematics and Computer Science,
Technical University of Denmark, DK-2800 Lyngby, Denmark.
E-mail pcha@dtu.dk, mads.friis.hansen@gmail.com.

January 11, 2014

[1]This work was supported by grant no. 274-07-0065 from the Danish Research Council for Technology and Production Sciences.

Abstract

In potential-field inversion problems, it can be difficult to obtain reliable information about the source distribution with respect to depth. Moreover, spatial resolution of the reconstructions decreases with depth, and in fact the more ill-posed the problem – and the more noisy the data – the less reliable the depth information. Based on earlier work using the singular value decomposition, we introduce a tool ApproxDRP which uses approximations of the singular vectors obtained by the iterative Lanczos bidiagonalization algorithm, making it well suited for large-scale problems. This tool allows a computational/visual analysis of how much the depth resolution in a computational potential-field inversion problem can be obtained from the given data. Through synthetic and real data examples we demonstrate that ApproxDRP, when used in combination with a plot of the approximate SVD quantities, may successfully show the limitations of depth resolution resulting from noise in the data. This allows a reliable analysis of the retrievable depth information and effectively guides the user in choosing the optimal number of iterations, for a given problem.

Keywords: Depth resolution, SVD analysis, iterative methods, Lanczos bidiagonalization.

Chapter 1

Introduction

Inverse potential-field problems are ill-posed by nature and hence they lack stability, implying that they are inherently difficult to solve because small perturbations of data lead to large perturbations of the solution. When solved on a computer, these difficulties lead to an inherent ill conditioning of the discretized problem $\boldsymbol{A}\,\boldsymbol{x} = \boldsymbol{b}$; see, e.g., Hansen [14] and Menke [20].

Regularization is needed to reduce the influence of the data errors, and regularization always amounts to suppressing certain components in the solution, namely, those most affected by the noise. For inverse potential-field problems these components are associated with deep sources, and therefore the regularization typically leads to a reduction of the depth-to-source resolution. *This paper deals with an efficient computational method to monitor the potential for depth resolution in a given problem with noisy data.* (We do not introduce any new regularization methods.)

If enough data are available to make the system $\boldsymbol{A}\,\boldsymbol{x} = \boldsymbol{b}$ square or overdetermined, then the matrix has – in principle – full rank and the (least squares) solution is therefore, in principle, unique. However, due to the ill conditioning, measurement errors and rounding errors often prevent us from computing a useful solution. Underdetermined systems, arising when less data are available, suffer from both ill conditioning and rank deficiency; their minimum-norm solution, in spite of being unique, is rarely useful because it lacks depth resolution [13]. A careful management of ill conditioning and rank deficiency, through the choice of regularization procedure, is crucial for obtaining reliable information about the source distribution with depth, cf. Fedi, Hansen & Paoletti [11], [12].

This work focuses on the analysis of depth resolution in classical regularization schemes such as Tikhonov regularization, which are described in, e.g., [14], [20], and [33]. In the last decade a variety of new methods have been proposed, and all of them seek to incorporate prior information in order to compute a more reliable and stable solution; see, e.g., [16], [26], [28], and [31]. It is a topic of future research how a depth resolution analysis can be applied to these methods.

The singular value decomposition (SVD) is a very powerful tool for analysis of inverse problems. For example, it is instrumental to monitor the singular values and the SVD coefficients, ie., the expansion coefficients of the right-hand side and the solution in the SVD

basis.

Fedi et al. [11] performed an SVD analysis of Tikhonov regularization, and they noticed that information about the deeper layers in the reconstruction are primarily associated with the smaller singular values. Hence, good depth resolution can only be obtained if enough singular vectors are available for inclusion in the regularized solution, i.e., if the noise level allows enough SVD components to be included.

With the aim of monitoring these aspects and, in particular, the possible depth resolution, Fedi et al. [11] introduced the *depth-resolution plot* (DRP). This is a simple graphical tool that allows a computational/visual analysis of how the depth resolution in a potential-field inversion problem is influenced by the noise and by the way the problem is discretized and regularized. The DRP is defined by means of the SVD and it shows what depth information is carried in each SVD component. The same basic idea was used by Pilkington [27] to monitor the available depth information in gradiometer inverse problems.

The aim of this paper is to introduce a new version of the DRP – called ApproxDRP – based on computationally attractive *approximations* of the singular vectors. The ApproxDRP is computed via an iterative method, and hence is suitable for large-scale potential-field inverse problems. When used in combination with a plot of approximate SVD quantities, the ApproxDRP may successfully show the limitations of depth resolution resulting from noise in the data. This allows a reliable analysis of the retrievable depth information that can guide the user in choosing the optimal number of iterations, for a given large-scale problem.

We emphasize that our goal is not to propose (yet) another numerical method for computing regularized solutions to large-scale inverse problems. We present an efficient computational analysis tool that provides important insight into the regularizing properties of known methods.

This report is organized as follows. Chapter 2 summarizes the SVD analysis of the problem, defines the DRP, and introduces different types of regularization terms in the Tikhonov formulation. In chapter 3 we introduce the iterative Lanczos bidiagonalization method used to compute the ApproxDRP, and we show its connection to the conjugate gradient method. Finally, in chapter 4 we give several examples of the use of ApproxDRP applied to problems with both synthetic and real data.

Chapter 2

Analysis of the Discretized Problem

In this chapter we introduce the necessary mathematical foundation that leads to the definition of the depth resolution plot, and we discuss variations of Tikhonov regularization. The outset is the linear system

$$\boldsymbol{A}\,\boldsymbol{x} \approx \boldsymbol{b}\ , \qquad \boldsymbol{A} \in \mathbb{R}^{\boldsymbol{m}\times\boldsymbol{n}}\ , \tag{2.1}$$

where the coefficient matrix $\boldsymbol{A}$ is obtained when the potential-field problem is discretized, the solution vector $\boldsymbol{x}$ represents the 3D reconstruction, and the right-hand side $\boldsymbol{b}$ is the measured data. In our analysis the particular discretization technique underlying (2.1) and the representation of the solution $\boldsymbol{x}$ are not important; also the system can be underdetermined, square, or overdetermined. More details about the SVD analysis can be found in several text books on regularization, such as [2], [10], [14], and [20].

2.1 SVD Analysis

Our analysis uses the singular value decomposition (SVD):

$$\boldsymbol{A} = \sum_{i=1}^{q} \boldsymbol{u}_i \sigma_i \boldsymbol{v}_i^T\ , \qquad q = \min(m,n) \tag{2.2}$$

where $\boldsymbol{u}_i$ and $\boldsymbol{v}_i$ are the left and right singular vectors (they are orthonormal), and σ_i are the singular values (they are nonnegative and appear in non-increasing order). Then a large class of regularization methods produce solutions of the form

$$\boldsymbol{x}_{\text{reg}} = \sum_{i=1}^{q} \phi_i \frac{\boldsymbol{u}_i^T \boldsymbol{b}}{\sigma_i}\, \boldsymbol{v}_i\ , \tag{2.3}$$

where ϕ_i are so-called filter factors associated with the particular regularization methods.

The role of the filter factors is effectively to dampen those noisy SVD components that correspond to small singular values. How many coefficient to include in $\boldsymbol{x}_{\text{reg}}$ can be determined, e.g., by inspecting a plot of σ_i, $|\boldsymbol{u}_i^T\boldsymbol{b}|$, and $|\boldsymbol{u}_i^T\boldsymbol{b}/\sigma_i|$ versus the index i, which we refer to as the *Picard Plot*. One should include only those SVD coefficients for which the Picard condition is satisfied, i.e., for which $|\boldsymbol{u}_i^T\boldsymbol{b}|$ decay faster than σ_i.

Since the regularized version $\boldsymbol{x}_{\text{reg}}$ represents a 3D reconstruction, it must be converted into an $n_x \times n_y \times n_z$ 3D array before it can be visualized, and this is done by a rearrangement of the elements. If $\boldsymbol{X}_{\text{reg}} \in \mathbb{R}^{n_x \times n_y \times n_z}$ is the 3D array associated with $\boldsymbol{x}_{\text{reg}} \in \mathbb{R}^n$, $n = n_x n_y n_z$, then we can use the notation

$$\boldsymbol{x}_{\text{reg}} = \text{vec}(\boldsymbol{X}_{\text{reg}}) \quad \Leftrightarrow \quad \boldsymbol{X}_{\text{reg}} = \text{vec}^{-1}(\boldsymbol{x}_{\text{reg}}) \ . \tag{2.4}$$

For the 3D reconstruction we then have the expression

$$\boldsymbol{X}_{\text{reg}} = \text{vec}^{-1}(\boldsymbol{x}_{\text{reg}}) = \sum_{i=1}^{q} \phi_i \frac{\boldsymbol{u}_i^T \boldsymbol{b}}{\sigma_i} \boldsymbol{V}_i \ , \tag{2.5}$$

in which

$$\boldsymbol{V}_i = \text{vec}^{-1}(\boldsymbol{v}_i) \ , \qquad i = 1, 2, \ldots, q \ . \tag{2.6}$$

Hence, the 3D reconstruction is expressed as a weighted sum of 3D "basis components" $\boldsymbol{V}_i$, each one derived from the corresponding right singular vector $\boldsymbol{v}_i$. Due to the filtering effect of the filter factors ϕ_i, the reconstruction is effectively composed of those "basis components" that correspond to the SVD components maintained.

For the important case of Tikhonov regularization, in which the regularized solution solves the problem

$$\min_{\boldsymbol{x}} \left\{ \|\boldsymbol{A}\,\boldsymbol{x} - \boldsymbol{b}\|_2^2 + \lambda^2 \|\boldsymbol{x}\|_2^2 \right\} , \tag{2.7}$$

it is well known that the filter factors are $\phi_i = \sigma_i^2/(\sigma_i^2 + \lambda^2)$ for $i = 1, \ldots, q$; they dampen SVD components for which $\sigma_i \ll \lambda$. For the truncated SVD (TSVD) method the filter factors are 1 and 0.

2.2 The Depth Resolution Plot

To better visualize and understand the depth information carried in each singular vector $\boldsymbol{v}_i$ – and the corresponding "basis component" $\boldsymbol{V}_i$ – Fedi et al. [11] introduced the Depth Resolution Plot (DRP) defined as follows. For each SVD component, define the corresponding vector $\boldsymbol{s}_i \in \mathbb{R}^{n_z}$ such that its ℓth element squared is the sum-of-squares of all the elements in the ℓth layer of $\boldsymbol{V}_i$:

$$(\boldsymbol{s}_i)_\ell^2 = \sum_{j=1}^{n_x} \sum_{k=1}^{n_y} (\boldsymbol{V}_i)_{jk\ell}^2 \ , \quad \ell = 1, \ldots, n_z \ , \quad i = 1, \ldots, q \ . \tag{2.8}$$

Since $\|\boldsymbol{s}_i\|_2 = \|\boldsymbol{v}_i\|_2 = 1$, it follows that each element of $\boldsymbol{s}_i$ is between 0 and 1, and the size of the ℓth element $(\boldsymbol{s}_i)_\ell$ shows how much the ith SVD component contributes to the ℓth layer in $\boldsymbol{X}_{\text{reg}}$. In particular, if $(\boldsymbol{s}_i)_\ell \ll 1$ then the ith SVD component contributes very little to the ℓth layer, and if $(\boldsymbol{s}_i)_\ell \approx 1$ then potentially the ith SVD component gives a large contribution to the ℓth layer.

We collect these vectors in an $n_z \times q$ matrix

$$\boldsymbol{S} = [\boldsymbol{s}_1, \boldsymbol{s}_2, \ldots, \boldsymbol{s}_q] \ . \tag{2.9}$$

A plot of this matrix, as an image, then gives a simple visualization of the contribution of all the SVD components to all the layers in $\boldsymbol{X}_{\text{reg}}$, and this is what we call the DRP. The rightmost plots in Fig. 4.3 in Section 4 show the typical appearance of a DRP: as the index i increases, the largest elements in $\boldsymbol{S}$ move from the top layer towards the bottom. The interpretation is that if only a few SVD components are included in $\boldsymbol{X}_{\text{reg}}$ then we can only recover shallow structures; as more SVD components are included we improve the depth resolution.

The particular depth, at which we can reliably obtain depth information, is determined by the number of SVD components that we can include in $\boldsymbol{X}_{\text{reg}}$ – as determined from the Picard Plot – and this depth is then easily monitored in the DRP. Together, the Picard Plot and the DRP provide an easy-to-use tool for visualizing the obtainable depth resolution is a given problem with noisy data. Specifically, the Picard Plot reveals *how many SVD components* can be included in the regularized solution – that is, it highlights the reliable components for which $|\boldsymbol{u}_i^T\boldsymbol{b}|$ decay faster than σ_i – and the DRP then shows *how much depth resolution* can be achieved with these SVD components.

2.3 Smoothness and Depth Weighting

We can incorporate prior information about the source in Tikhonov regularization, in order to compute improved solutions. For example, it is well known that we can impose smoothness on the solution if in (2.7) we replace the regularization term $\|\boldsymbol{x}\|_2^2$ with a term of the form $\|\boldsymbol{L}\,\boldsymbol{x}\|_2^2$, where the matrix $\boldsymbol{L}$ is a discrete approximation to a derivative operator; see, e.g., [11] and [14].

Following Li & Oldenburg [17], [18], we can also incorporate so-called depth weighting in the Tikhonov formulation. To do this we introduce a diagonal matrix $\boldsymbol{W}$ whose diagonal elements give a weight to each element in $\boldsymbol{x}$ that is related to its depth, and then the regularization terms takes the form $\|\boldsymbol{W}\boldsymbol{x}\|_2^2$ or $\|\boldsymbol{W}\boldsymbol{L}\,\boldsymbol{x}\|_2^2$. The particular choice of the weighting is discussed in [7] and [24], where it is shown that a careful choice of weighting can indeed improve the depth-to-source resolution. A key idea is to define the exponent s of the depth weighting function

$$w(z) = (h + |z|)^{-s}, \quad h = \text{height of data points} \tag{2.10}$$

such that $\beta = 2s$ fits the fall-off rate of the field, determined by a direct estimate of the structural index; this approach is a variation of that by Li & Oldenburg [17], [18] who used a pre-determined fixed value of s.

Tikhonov problems of the general form

$$\min_{\boldsymbol{x}} \left\{ \|\boldsymbol{A}\,\boldsymbol{x} - \boldsymbol{b}\|_2^2 + \lambda^2 \|\boldsymbol{M}\boldsymbol{x}\|_2^2 \right\}, \tag{2.11}$$

where $\boldsymbol{M}$ is a general matrix (such as the identity, $\boldsymbol{L}$, or $\boldsymbol{W}\boldsymbol{L}$), can be analyzed by means of the generalized SVD (GSVD), cf. [14]. The key result is that a canonical expression similar to (2.3) still holds, now with $\boldsymbol{u}_i$ and $\boldsymbol{v}_i$ being the left and right *generalized* singular vectors of the matrix pair $(\boldsymbol{A}, \boldsymbol{M})$; we note that the latter are not orthonormal, see [11] for details.

Hence, the DRP based on the matrix $\boldsymbol{S}$ is a general tool for studying depth resolution also when smoothness and depth weighting is used.

Analogous to this, Pilkington [27] used the eigenvectors of $\boldsymbol{A}^T\boldsymbol{A} + \lambda^2\boldsymbol{M}^T\boldsymbol{M}$ to study depth resolution in gradiometer inverse problems. While the eigenvectors are not identical to generalized right singular vectors of $(\boldsymbol{A}, \boldsymbol{M})$, his analysis is conceptually similar to ours. In particular, Fig. 7 is his paper demonstrates how shallow and deep sources are represented by eigenvectors corresponding to large and small eigenvalues, respectively.

Chapter 3

Large-Scale Problems and ApproxDRP

While the SVD is a very important tool for analysis of discretezed inverse problems, it is only useful for problems where it is feasible to compute the SVD. In this chapter we describe a favorable alternative based on a classical iterative algorithm.

3.1 CGLS and Krylov Subspaces

For large-scale problems one must turn to iterative methods that avoid factorization of the matrix $\boldsymbol{A}$, such as CGLS which is a stable implementation of the conjugate gradient (CG) algorithm applied to linear least squares problems. This iterative approach to solving large-scale problems sets the stage for the derivation of the approximate DRP.

There are two different ways to use the CGLS algorithm to compute regularized solutions to inverse problems:

1. We can apply CGLS to the Tikhonov problem (2.7) or (2.11), both of which are linear least squares problems.
2. We can apply CGLS to the un-regularized least squares problem $\min_{\boldsymbol{x}} \|\boldsymbol{A}\,\boldsymbol{x} - \boldsymbol{b}\|_2^2$ and use the fact that the number of iterations plays the role of a regularization parameter.

To understand the latter approach, which is sometimes referred to as "regularizing iterations" [14] we must consider the associated Krylov subspace, defined as

$$\mathcal{K}_k \equiv \text{span}\{\boldsymbol{A}^T\boldsymbol{b}, \boldsymbol{A}^T\boldsymbol{A}\,\boldsymbol{A}^T\boldsymbol{b}, \ldots, (\boldsymbol{A}^T\boldsymbol{A})^{k-1}\boldsymbol{A}^T\boldsymbol{b}\}\ , \tag{3.1}$$

which is a linear subspace of dimension $\leq k$. Then it can be shown [4] that the CGLS iteration vector $\boldsymbol{x}^{(k)}$ after k iterations is mathematically equivalent to the solution to the constrained problem

$$\min \|\boldsymbol{A}\,\boldsymbol{x} - \boldsymbol{b}\|_2^2 \quad \text{subject to} \quad \boldsymbol{x} \in \mathcal{K}_k\ . \tag{3.2}$$

(This is, of course, not how CGLS is implemented.) It is well understood that the projection onto the Krylov subspace has a regularizing effect. This is related to the fact that this

subspace can be considered a rough approximation to the subspace span$\{\boldsymbol{v}_1, \ldots, \boldsymbol{v}_k\}$ spanned by the first k right singular vectors; see, e.g., [10] and [14]. We provide more details about this aspect below.

3.2 Lanczos Bidiagonalization and SVD Approximations

There is an alternative, iterative algorithm that can be used to compute CGLS solutions, and which explicitly constructs an orthonormal basis for the Krylov subspace $\mathcal{K}_k$. This algorithm is known as LSQR [21] and it is based on the so-called *Lanczos bidiagonalization algorithm* defined by:

$\beta_1 \, \boldsymbol{u}_1^{\mathsf{L}} = \boldsymbol{b}$
$\alpha_1 \, \boldsymbol{v}_1^{\mathsf{L}} = \boldsymbol{A}^T \boldsymbol{u}_1^{\mathsf{L}}$
for $k = 1, 2, \ldots, K$
  $\beta_{k+1} \boldsymbol{u}_{k+1}^{\mathsf{L}} = \boldsymbol{A} \, \boldsymbol{v}_k^{\mathsf{L}} - \alpha_k \boldsymbol{u}_k^{\mathsf{L}}$
  $\alpha_{k+1} \boldsymbol{v}_{k+1}^{\mathsf{L}} = \boldsymbol{A}^T \boldsymbol{u}_{k+1}^{\mathsf{L}} - \beta_{k+1} \boldsymbol{v}_k^{\mathsf{L}}$
end

where K is the number of Lanczos iterations. If we construct the two matrices with orthonormal columns

$$\boldsymbol{U}_{k+1}^{\mathsf{L}} = [\boldsymbol{u}_1^{\mathsf{L}}, \ldots, \boldsymbol{u}_{k+1}^{\mathsf{L}}] \; , \quad \boldsymbol{V}_k^{\mathsf{L}} = [\boldsymbol{v}_1^{\mathsf{L}}, \ldots, \boldsymbol{v}_k^{\mathsf{L}}] \; ,$$

and the $(k+1) \times k$ bidiagonal matrix

$$\mathbf{B}_{\mathbf{k}}^{\mathsf{L}} = \begin{pmatrix} \alpha_1 & & & \\ \beta_2 & \alpha_2 & & \\ & \beta_3 & \ddots & \\ & & \ddots & \alpha_k \\ & & & \beta_{k+1} \end{pmatrix} \; ,$$

then the CGLS solution is given by

$$\boldsymbol{x}^{(k)} = \boldsymbol{V}_k^{\mathsf{L}} \mathbf{y}_{\mathbf{k}} \; , \qquad \mathbf{y}_{\mathbf{k}} = \text{argmin}_{\mathbf{y}} \|\mathbf{B}_{\mathbf{k}}^{\mathsf{L}} \, \mathbf{y} - \beta_{\mathbf{1}} \mathbf{e}_{\mathbf{k+1}}\|_{\mathbf{2}}^{\mathbf{2}} \; , \tag{3.3}$$

where $\mathbf{e}_{\mathbf{k+1}} = (\mathbf{1}, \mathbf{0}, \ldots, \mathbf{0})^{\mathbf{T}} \in \mathbb{R}^{\mathbf{k+1}}$. This approach is known to be very robust to rounding errors, and the work involved in solving the least squares problem in (3.3) is negligible. The Lanczos bidiagonalization algorithm is closely related to the Partial Least Squares algorithm used in statistics [19], [32].

Our main interest in the Lanczos algorithm comes from the fact that it also provides partial approximations to the SVD of $\boldsymbol{A}$. For any $k \leq K$, let the SVD of the bidiagonal matrix be given by

$$\mathbf{B}_{\mathbf{k}}^{\mathsf{L}} = \mathbf{P}_{\mathbf{k+1}} \mathbf{\Omega}_{\mathbf{k}} \mathbf{Q}_{\mathbf{k}}^{\mathbf{T}} \; ,$$

and define the two matrices with orthonormal columns

$$\widetilde{\boldsymbol{U}}_{k+1} = \boldsymbol{U}_{k+1}^{\mathsf{L}} \mathbf{P}_{\mathbf{k+1}} \; , \quad \widetilde{\boldsymbol{V}}_{\mathbf{k}} = \boldsymbol{V}_{\mathbf{k}}^{\mathsf{L}} \mathbf{Q}_{\mathbf{k}} \; .$$

Then it can be shown [4] that the singular values $\tilde{\sigma}_i$ of $\mathbf{\Omega_k}$ are approximations to the k largest singular values σ_i of $\boldsymbol{A}$, and the columns $\tilde{\boldsymbol{u}}_i$ and $\tilde{\boldsymbol{v}}_i$ of $\widetilde{\boldsymbol{U}}_{k+1}$ and $\widetilde{\boldsymbol{V}}_k$ are approximations to the corresponding left and right singular vectors of $\boldsymbol{A}$. Moreover, as k increases the largest singular values $\tilde{\sigma}_i$, and the corresponding $\tilde{\boldsymbol{u}}_i$ and $\tilde{\boldsymbol{v}}_i$, become increasingly better approximations to the corresponding singular values and vectors.

Due to the above convergence properties, it is clear that the CGLS solutions $\boldsymbol{x}^{(k)}$ are regularized solutions because they are dominated by those SVD components that correspond to the large singular values – similar to Tikhonov solutions to (2.7) as well as truncated SVD solutions. This fact makes the CGLS and LSQR methods attractive for large-scale regularization problems [14] and they are used, e.g., in image deblurring [8] and tomography [15].

3.3 Approximate Picard Plot and ApproxDRP

The above properties allow us to efficiently compute approximations to those SVD components that take part in computing the regularized solution, namely, those associated with the larger singular values. Specifically, after K Lanczos iterations we can compute an approximate Picard Plot associated with the singular values with index $i = 1, \ldots, K$. Moreover, by substituting $\tilde{\boldsymbol{v}}_i$ for $\boldsymbol{v}_i$ in the definition of the DRP from §2.2, we can compute a corresponding approximate DRP

$$\widetilde{\boldsymbol{S}}_K = [\tilde{\boldsymbol{s}}_1, \tilde{\boldsymbol{s}}_2, \ldots, \tilde{\boldsymbol{s}}_K] \tag{3.4}$$

where the elements of the ith column $\tilde{\boldsymbol{s}}_i$ are given by

$$(\tilde{\boldsymbol{s}}_i)_\ell^2 = \sum_{j=1}^{n_x} \sum_{k=1}^{n_y} (\widetilde{\boldsymbol{V}}_i)_{jk\ell}^2 \ , \quad \ell = 1, \ldots, n_z \ , \quad i = 1, \ldots, K \tag{3.5}$$

in which $\widetilde{\boldsymbol{V}}_i = \mathrm{vec}^{-1}(\tilde{\boldsymbol{v}}_i)$. We refer to the plot of $\widetilde{\boldsymbol{S}}_K$ as ApproxDRP because it contains a partial approximation to the DRP.

Some of the columns of the ApproxDRP matrix $\widetilde{\boldsymbol{S}}_K$ are very good approximations to the corresponding columns of the true DRP, namely, those corresponding to the larger singular values. These are the columns in the left part of $\widetilde{\boldsymbol{S}}_K$. On the other hand, the columns in the right part of $\widetilde{\boldsymbol{S}}_K$ are less good approximations to those of $\boldsymbol{S}$. Hence we cannot expect the ApproxDRP to closely resemble the SVD-based DRP (if we could compute it) – in fact they may appear somewhat different but with the same overall structure. At any rate, we emphasize that the information in ApproxDRP correspond to the actual basis vectors for the CGLS solution $\boldsymbol{x}^{(k)}$, and hence they are still relevant for the study of the depth resolution in $\boldsymbol{x}^{(k)}$.

A few words about the numerical implementation of the above procedure. We found that in order to minimize the effect of rounding errors, we need to orthonormalize the columns of the matrix $\boldsymbol{V}_k^{\mathsf{L}}$. There are adaptive ways to do this only when needed; in our model implementation we do it in every iteration. We do not need to orthonormalize the columns of $\boldsymbol{U}_{k+1}^{\mathsf{L}}$ since this matrix is not needed explicitly in the algorithm; the quantities $\tilde{\boldsymbol{u}}_i^T \boldsymbol{b}$ in the Picard plot can be computed efficiently "on the fly" during the iterations.

To summarize, the Lanczos bidiagonalization algorithm with K iterations allows us to compute an approximate Picard Plot for the leading K SVD components, a corresponding approximate DRP for the same K components, as well as all CGLS solutions $\boldsymbol{x}^{(k)}$ for $k = 1, \ldots, K$, for the price of a single Lanczos bidiagonalization process with K iterations. The amount of work is about $4mnK + 4nK^2$ arithmetic operations, and the storage requirements – in additional to storage for the matrix $\boldsymbol{A}$ – are dominated by nK matrix elements for the matrix $\widetilde{\boldsymbol{V}}_K$.

A further advantage of the above computational approach is that we can use the analysis of the ApproxDRP and the associated approximation Picard Plot as a means for choosing the optimal dimension k of the Krylov subspace underlying the CGLS solution $\boldsymbol{x}^{(k)}$. This, in turn, acts as a means for choosing the optimal number of CGLS iterations; the requirement for this to work is that K is chosen large enough that we can determine an optimal $k \leq K$. The process of computing a regularized solution within the Krylov subspace $\mathcal{K}_K$ is sometimes referred to as a "hybrid method" [8], [14].

3.4 Bidiagonalization with Preconditioning for GSVD Approximations

We shall now demonstrate how to easily modify the Lanczos bidiagonalization algorithm to compute CGLS solutions $\boldsymbol{x}^{(k)}$ that resemble solutions to the Tikhonov problem (2.11) with a general regularization term $\|\boldsymbol{M}\boldsymbol{x}\|_2^2$, where $\boldsymbol{M} = \boldsymbol{L}$, $\boldsymbol{W}$, or $\boldsymbol{W}\boldsymbol{L}$, cf. §2.3. At the same time we can compute the necessary approximate GSVD quantities that allow us to produce the associated approximate Picard Plot and ApproxDRP for these solutions.

If we introduce the new variable $\boldsymbol{\xi} = \boldsymbol{M}\boldsymbol{x}$ then the general-form Tikhonov problem (2.11) takes the form

$$\min_{\boldsymbol{\xi}} \left\{ \|(\boldsymbol{A}\boldsymbol{M}^{-1})\,\boldsymbol{\xi} - \boldsymbol{b}\|_2^2 + \lambda^2 \|\boldsymbol{\xi}\|_2^2 \right\} \ . \tag{3.6}$$

Applying the Lanczos bidiagonalization algorithm to the above problem yields iteration vectors $\boldsymbol{\xi}^{(k)}$ as well as the matrices $\widetilde{\boldsymbol{U}}_{k+1}$, $\widetilde{\boldsymbol{V}}_k$ and $\boldsymbol{\Omega}_{\mathbf{k}}$ from §3.2. From the analysis in [14] it then follows that:

1. The desired iteration vectors are $\boldsymbol{x}^{(k)} = \boldsymbol{M}^{-1}\boldsymbol{\xi}^{(k)}$.
2. The approximate generalized singular values are the diagonal elements of $\boldsymbol{\Omega}_{\mathbf{k}}$.
3. The approximate GSVD vectors are the columns of $\widetilde{\boldsymbol{U}}_{k+1}$ and $\boldsymbol{M}^{-1}\widetilde{\boldsymbol{V}}_k$.

The matrix $\boldsymbol{M}^{-1}$ acts as a *preconditioner* for the iterative algorithm. Due to the sparsity of $\boldsymbol{L}$ and $\boldsymbol{W}$ there is little computational overhead in the operations with $\boldsymbol{M}^{-1}$ and hence we have an efficient iterative algorithm to handle a general regularization term $\|\boldsymbol{M}\boldsymbol{x}\|_2^2$. In particular, we can easily compute the approximate Picard Plot and ApproxDRP from the approximate GSVD quantities.

Chapter 4

Computed Examples

We now give several examples of the use of the ApproxDRP for analysis of depth resolution in potential field inverse problems. We first show two small problems where we compare the results from the SVD and the approximated SVD; we illustrate that the use of the iterative algorithm can produce good approximations to the Picard plot and the DRP as well as reliable reconstructions. Then we present results for a larger problem whose dimensions make the use of SVD impractical, and we finish with a problem using real data.

Throughout this chapter we use white Gaussian noise scaled such that $\|\mathbf{e}\|_2/\|\boldsymbol{b}\|_2 = \eta$, where $\mathbf{e}$ is the vector of perturbations; we refer to η as the relative noise level. When depth weighting is used is has the form (2.10) with different choices of the exponent. When smoothing is used the matrix $\boldsymbol{L}$ always represents a linear combination of the 2-norm of the solution and the 2-norm of its second partial derivative in the z-direction (see Eq. (14) in [11] where the same smoothing was used).

4.1 Validation of ApproxDRP on a Very Small Problem

Our first example is a small 3D gravity test problem whose source volume has dimensions $1\,\text{km} \times 1\,\text{km} \times 0.4\,\text{km}$; it is discretized with $N_x = N_y = 10$ and $N_z = 4$, i.e., the solution consists of $n = 400$ cells. The data points are arranged in a 25×25 grid (i.e., $m = 625$), covering an area of $1\,\text{km} \times 1\,\text{km}$, and they are located on the ground level. This leads to an overdetermined problem.

Figure 4.1 shows a comparison of the SVD-based DRP with the approximate DRP obtained via the Lanczos bidiagonalization algorithm. The two plots are very similar, showing that the iterative algorithm provides very good SVD approximations for this small problem. Both DRPs show that, for this test problem without noise, the inclusion of 400 SVD components, and using $k = 400$ iterations, allows reliable reconstructions to a depth of 0.4 km.

The source in this example is a box with density of $1\,\text{g/cm}^3$ and dimensions $0.3\,\text{km} \times 0.3\,\text{km} \times 0.1\,\text{km}$ whose center is located at 0.3 km depth, see Fig. 4.2. Consider first the case of no noise; the optimal regularization parameters (the SVD truncation parameter and the number of CGLS iterations) were chosen on the basis of the SVD-based Picard Plot and the approximate Picard Plot (Fig. 4.2 middle left), and the reconstructions from to the

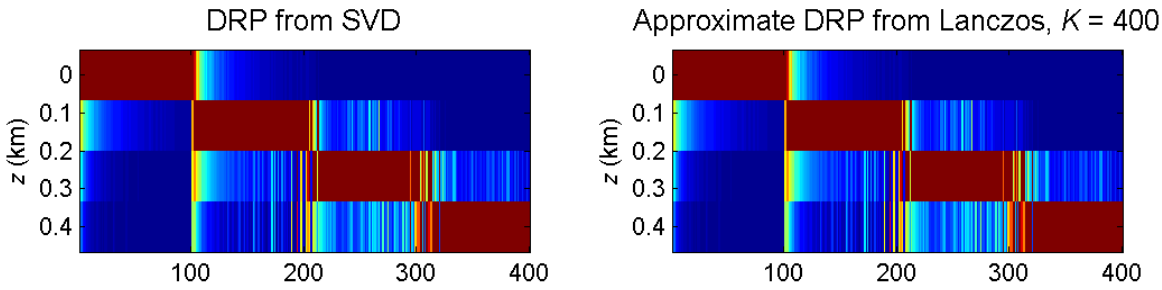

Figure 4.1: Example 4.1. Comparison of the SVD-based DRP (left) with the approximate DRP (right) obtained using the Lanczos bidiagonalization algorithm with a maximum of $K = 400$ iterations. The results are almost indistinguishable for this small problem.

two methods are shown in the bottom left of Fig.4.2. We notice that the CGLS solution (obtained via the Lanczos algorithm) is almost indistinguishable from that obtained by the SVD method, and both solutions reconstruct very well the position and extent of the source.

Now consider the case of noisy data, with relative noise level $\eta = 10^{-4}$. The right middle part of Fig. 4.2 shows the SVD-based Picard Plot and the approximate Picard Plot for the noisy data; the right-hand-side coefficients $\boldsymbol{u}_i^T \boldsymbol{b}$ now level off at a plateau around the noise level for $i > 300$ SVD components and for $k > 230$ iterations. Thus, the considered level of noise allows the inclusion of at most 300 SVD components and 230 CGLS iterations. This leads to reliable reconstructions down to a depth slightly greater than 0.3 km (compare with Fig 4.1); any structure in the computed solution below this depth cannot be fully trusted. Nevertheless we note that, even with the limitation connected to the presence of noise, both regularized reconstructions show rather clearly the position and depth of the source. We conclude that the use of the bidiagonalization algorithm leads to reconstructions fairly comparable with those achieved by SVD.

4.2 Another Comparison of DRP and ApproxDRP

Our second example is a larger 3D gravity problem, and we compare again use of the SVD and the approximate SVD. For this larger problem we do not expect the ApproxDRP to closely resemble the SVD-based DRP. In addition to the SVD and Lanczos methods, we also consider the use of combined smoothing and depth weighting with $\boldsymbol{W}$ representing the depth weighting function (2.10) with $s = 1$; this is treated by means of GSVD and preconditioning as discussed in §3.4.

The source volume has dimensions 10 km × 10 km × 3 km, discretized with $N_x = N_y = 20$ and $N_z = 10$, i.e., the solution domain consists of $n = 4,000$ cells. The data points are arranged in a 60×60 grid ($m = 3,600$), covering an area of 10 km × 10 km, and they are measured at the ground level. This leads to a slightly under-determined problem.

The source is made of a box with density of 1 g/cm^3 and dimensions 0.5 km × 0.5 km × 0.3 km with the center at 5 km along x and y and at the depth 1.2 km. The relative noise level is $\eta = 10^{-5}$. The top of Fig. 4.4 shows the source and its gravity field.

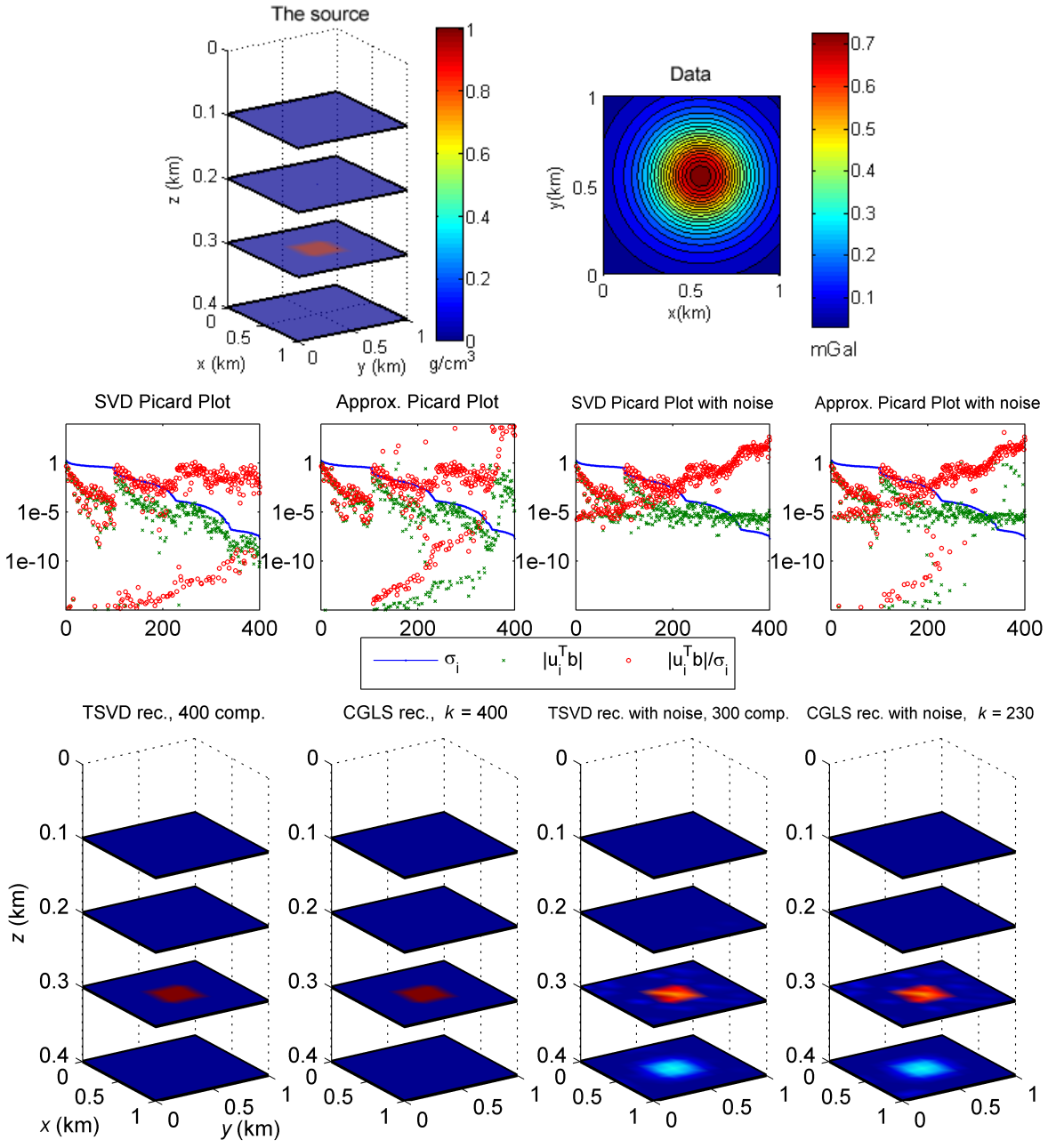

Figure 4.2: Example 4.1. Comparison of SVD and approximate SVD for the same small test problem as in Fig. 4.1. Top: source model and corresponding gravity field. Middle, left to right: SVD-based Picard Plot, approximate Picard Plot from Lanczos, SVD-based Picard Plot with white noise added to the data with relative noise level $\eta = 10^{-4}$), and approximate Picard Plot with noisy data. Bottom, left to right: truncated SVD reconstruction with 400 SVD components and no noise, CGLS reconstruction obtained by the Lanczos algorithm with $k = 400$ iterations and no noise, truncated SVD reconstruction with 300 SVD components and noisy data, and CGLS reconstruction for noisy data obtained by the Lanczos algorithm with $k = 230$ iterations.

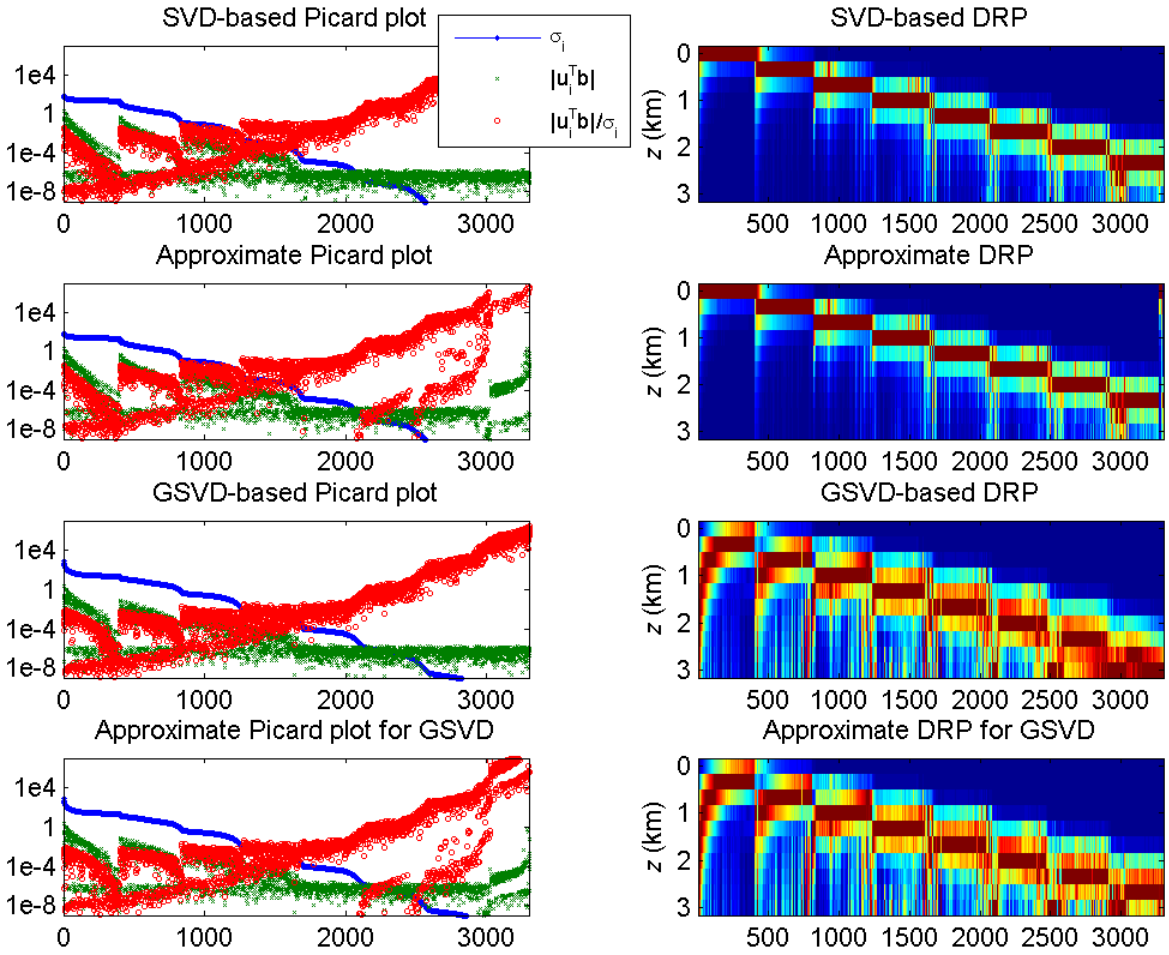

Figure 4.3: Example 4.2. Left: the Picard Plots based on SVD and GSVD as well as on the (preconditioned) Lanczos bidiagonalization method. Right: the corresponding DRPs.

Consider first the case with no depth weighting. The optimal regularization parameters for this problem (the SVD truncation parameter and the number of CGLS iterations) were chosen on the basis of the SVD-based Picard Plot and the approximate Picard Plot, cf. the two top left plots in Fig. 4.3. These plots show that the Picard condition is satisfied for up to 1700 SVD components and for up to 1650 iterations, at which point the right-hand-side coefficients $\boldsymbol{u}_i^T \boldsymbol{b}$ level off at a plateau around the noise level. Thus, the considered level of noise allows the inclusion of at most 1700 SVD components and 1500 CGLS iterations.

The right plots of Fig. 4.3 show the SVD-based DRP and the ApproxDRP; the theory predicts that we can expect them to be somewhat different, but the overall structure is precisely the same. Thee plots show that the inclusion of the above-mentioned number SVD components and iterations allows reliable reconstructions down to a depth of about 1.8 km for both cases. The middle part of Fig. 4.4 shows the reconstructions obtained with these optimal regularization parameters.

Next we consider the case where smoothing and depth weighting was used, cf. the bottom half of Fig. 4.3. Again the GSVD-based DRP and the ApproxDRP with computed with preconditioning are somewhat different (as predicted by the theory), and again they exhibit the same overall structure. By including 2000 GSVD coefficients and 1650 preconditioned iterations, we expect a reliable reconstruction down to a depth of about 1 km; these solutions are shown in the bottom of Fig. 4.4.

We conclude that the standard and preconditioned CGLS reconstructions are comparable with those obtained by the truncated SVD/GSVD methods and that all reconstructions show very well the position and extent of the source. This confirms the conclusions drawn for the previous small example, namely, the use of the iterative Lanczos bidiagonalization algorithm allows reconstructions comparable with those achieved by SVD/GSVD.

4.3 A Larger Problem: Lanczos Bidiagonalization Only

In this example we use ApproxDRP for studying how much depth resolution can be achieved in a larger test problem whose dimensions make the use of the SVD impractical. We consider a 3D source volume with dimensions 1 km $\times$ 1 km $\times$ 0.5 km discretized with $N_x = N_y = 50$ and $N_z = 30$, i.e., the solution domain consists of $n = 75,000$ cells. The data points, covering an area of 1 km $\times$ 1 km, and measured 1 m above the ground, are arranged in an 80×80 grid ($m = 6,400$), i.e., the problem is now severely under-determined.

The source is a box with magnetization 1 A/m and dimensions 0.14 km $\times$ 0.14 km $\times$ 0.1 km and its top is located at 0.12 km depth. Again, we added white Gaussian noise to the data with a relative noise level 10^{-5}.

Figure 4.5 shows the approximate Picard Plot, the approximate DRP, the synthetic source and its field, and the reconstruction obtained by the Lanczos bidiagonalization algorithm. For this example we used both smoothing and depth weighting with the exponent $s = 1.4$, corresponding to a structural index of 2.8 (the analysis leading to this choice is not included in this paper).

The approximate Picard plot shows that the low noise in the data allows the use of all $K = 6300$ iterations. At the same time, the approximate DRP shows that a large part of

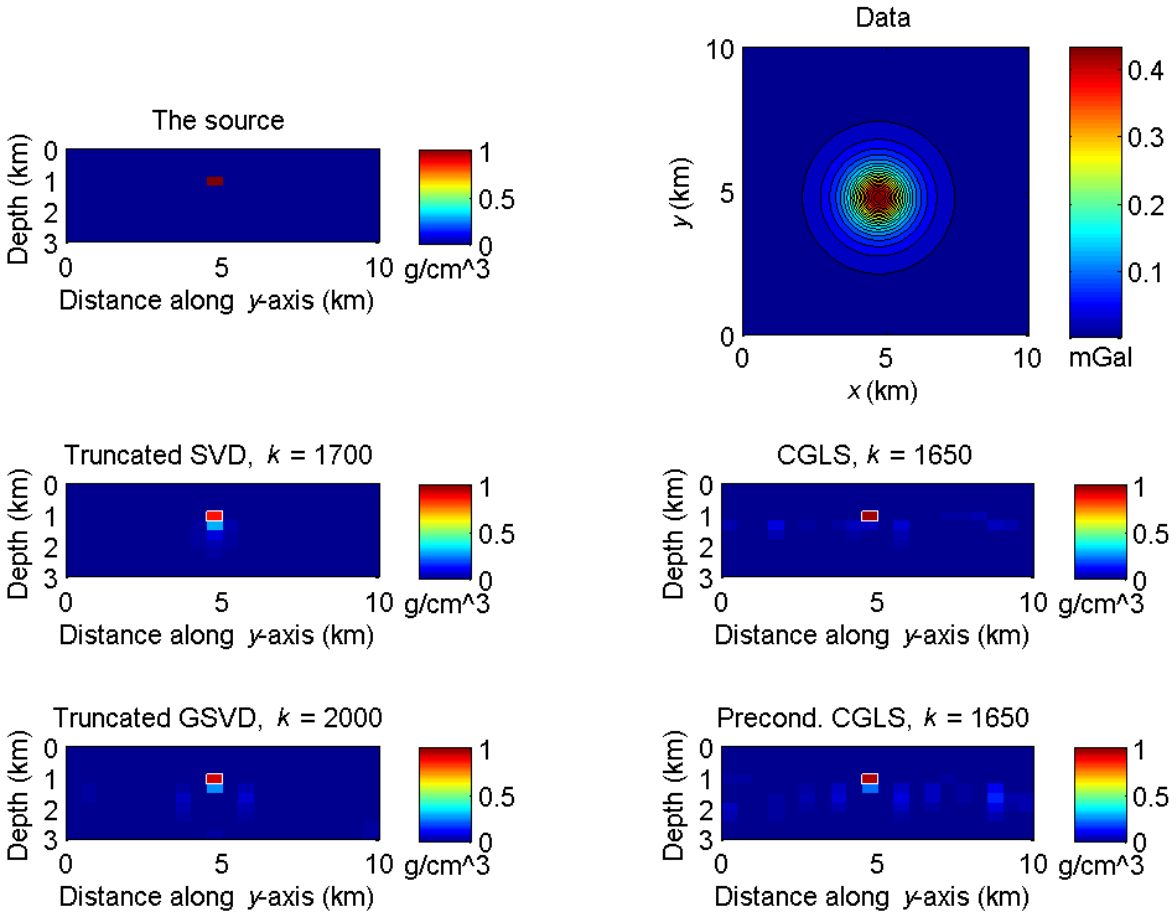

Figure 4.4: Example 4.2. Top: the source and its gravity field; all source plots shows the middle slice along the y-z-direction. Middle: the reconstructions computed by means of truncated SVD and CGLS, using the optimal regularization parameters from Fig. 4.3. Bottom: reconstructions by means of truncated GSVD and preconditioned CGLS for the case with both smoothing and depth weighting.

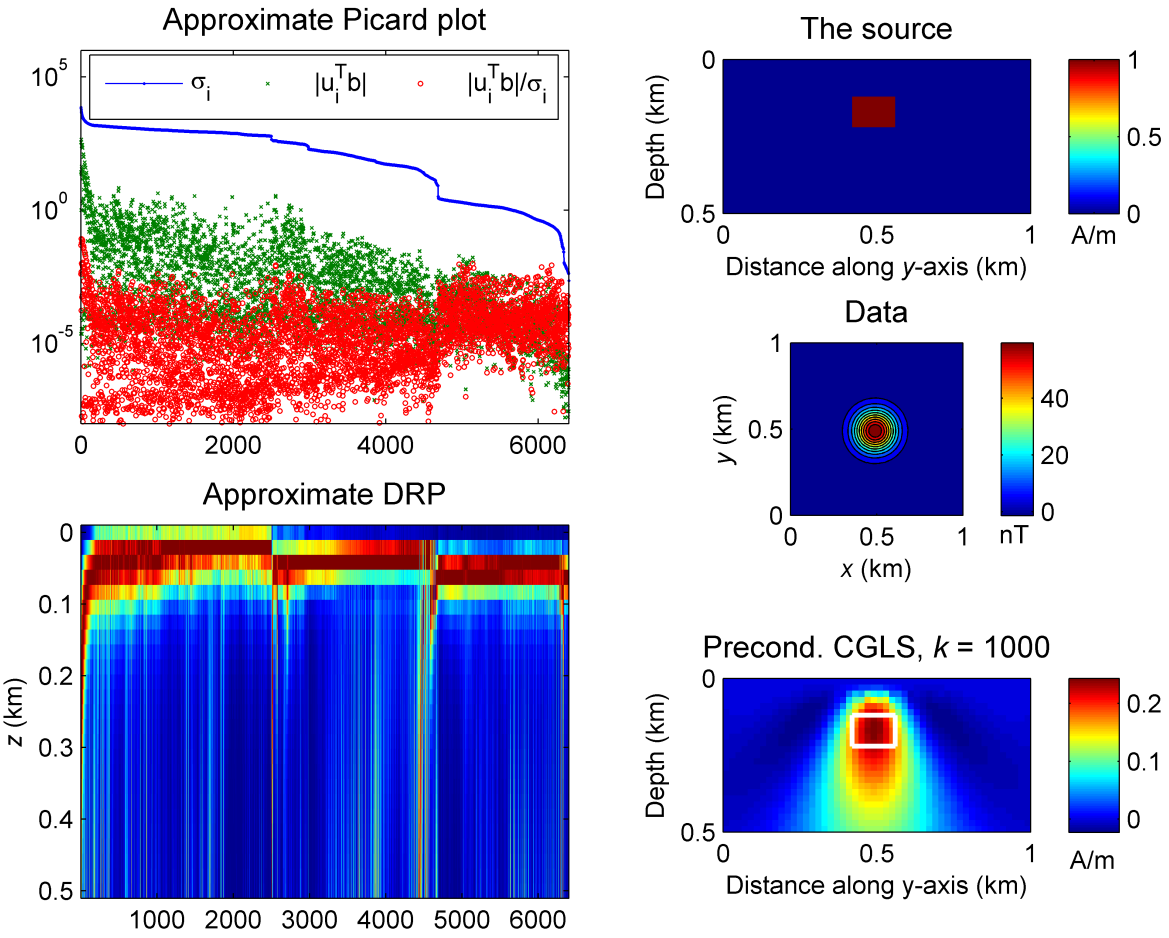

Figure 4.5: Example 4.3. Left: analysis by means of the Lanczos bidiagonalization algorithm. Right: the source and its magnetic field, as well as the CGLS reconstruction using $k = 1000$ iterations.

the depth information is actually carried on the first 1000 approximate singular vectors, and their inclusion in the reconstruction makes it possible to retrieve reliable information about the magnetization distribution down to a depth of about 0.2 km.

Despite that the reconstruction looks blurred and relatively weak in strength, which is due to the highly underdetermined nature of the problem, we notice that the reconstruction depicts rather well the depth position of the source. An improved solution with more focused reconstructions may be obtained by introducing further a priori information, such as positivity constraints and the source edge positions, as shown in [24]. The formulation of depth resolution analysis tools for constrained problems is a topic of future research.

4.4 Real Data Example: The Campanian Plain Gravity Field

As a real case application of the Lanczos bidiagonalization mehtod and ApproxDRP we considered the inverse problem of computing the density contrasts from measurements of the gravity field in the Campanian Plain (southern Italy). The Campanian Plain is a Plio-Quaternary NW-SE trending graben of size 2000 km^2, bordered by Mesozoic limestone mountains, cf., e.g., [30]. The maximum depth of limestone is more than 4 km b.s.l. and the plain is filled with alluvial and volcanic materials down to at least 3 km depth [1].

Several geophysical surveys, mainly gravimetric, magnetic, and seismic, were carried out in the Campanian Volcanic Area [23], [25]. A compilation of gravity data of the Campanian Plain [6] shows a wide low area, divided in three small minima (Volturno, Acerra, and Pompei) by the maxima of Parete and Mt. Somma-Vesuvius. The Acerra gravity low was interpreted by potential field studies [29], [22] as due to both shallow and intermediate-depth sources. The field attributed to intermediate-depth sources (with a wavelength in the range 40–100 km) is characterized by a broad low in correspondence with the town of Naples and the authors interpreted it as connected to low density molten trachybasalts between 8 km and 12 km with a density contrast with respect to the surrounding crystalline rocks of about $-0.2\,\mathrm{g/cm}^2$.

The location and the dimensions of this reservoir led Rapolla et al. to hypothesize that it may be feeding the eruptive centers of the whole Campanian volcanic region. Those results were later confirmed by seismic studies carried out in the Neapolitan volcanic area, cf., e.g., [3], [34], [35], which recognized a low-velocity layer with an almost flat surface and a depth-to-the-top of 8–10 km, whose area is at least 400 km^2. These studies found that the S- and P-wave velocities below the interface are consistent with velocities expected for a partially molten body hosted in a densely fractured volume of rock and their results also support the gravity-based hypothesis of a single continuous magma reservoir feeding the Neapolitan volcanic area.

The purpose of our investigation is to apply our iterative method and the associated analysis technique to this interesting case. Figure 4.6 shows the vertical derivative of the same gravity field low used by Rapolla et al. [29] for studying the intermediate sources. This field is characterized by an extended low with an amplitude of about 30 mGal/km that appears to be stretched southwest to northeast, with its center located near the city of Naples. According to Poisson's equation [5, §5.4] the vertical derivative of the gravity field from a uniform density source is equivalent to the field from a source with uniform magnetization,

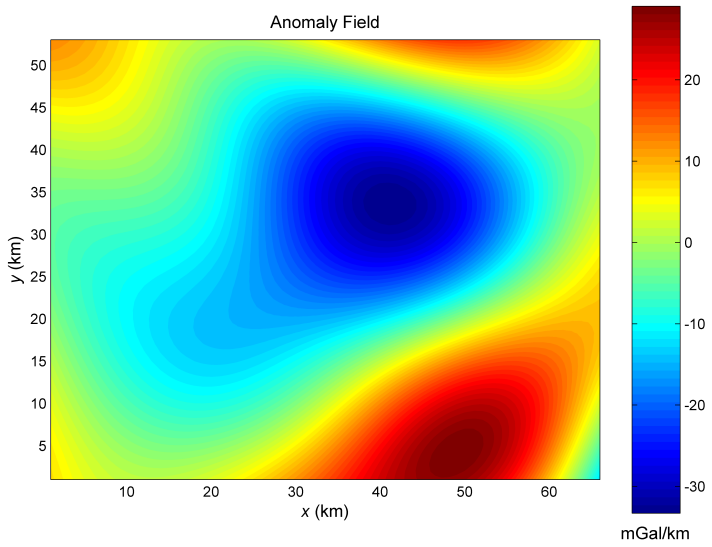

Figure 4.6: Example 4.4. Vertical derivative of the gravity field in the Campanian Plain, (southern Italy).

provided that both the inducing field and the direction of magnetization of the source are vertical. Thus, we treated this problem as a magnetization problem and we applied the analysis from the previous chapters to interpret the vertical derivative of this gravity data set.

For the analysis of this data set we again use both smoothing and depth weighting. As the analyzed anomaly field is characterized by the contribution of sources of different depth/dimension, the correct structural index (and so the depth weighting exponent) is expected to be spatially varying. Thus, we preferred to choose the depth weighting exponent based on geological/geophysical constraints, such as the depth-to-the-top of the low density structure (cf., e.g., [29], [34]) and the depth of the Moho [9]. This led to a structural index of 1.4 and thus an exponent $s = 0.7$ in the depth weighting function.

The source volume covers a horizontal area of 65 km $\times$ 65 km with depths ranging from 0 km to 26 km below the surface. This volume was divided into a $40 \times 40 \times 30$ grid of cells. The total area covered by the data set is 56 km $\times$ 56 km with a data spacing of 1 km along both directions.

The approximate Picard plot, the ApproxDRP, and the reconstruction for this problem are shown in Fig. 4.7. For this analysis we used a maximum of $K = 2500$ iterations, but for clarity we only include the first 200 components in the ApproxDRP. The approximate Picard plot shows that the noise in the data allows the use of all iterations ($k = K$). The ApproxDRP shows that a large part of the depth information is actually carried in the first 40–50 approximate singular vectors, and with just $k = 200$ iterations it is possible to retrieve reliable information about the density distribution down to a depth of about 26 km, that is, to the bottom of the discretized domain.

The reconstruction in the right part of Fig. 4.7, using only 200 iterations, shows the

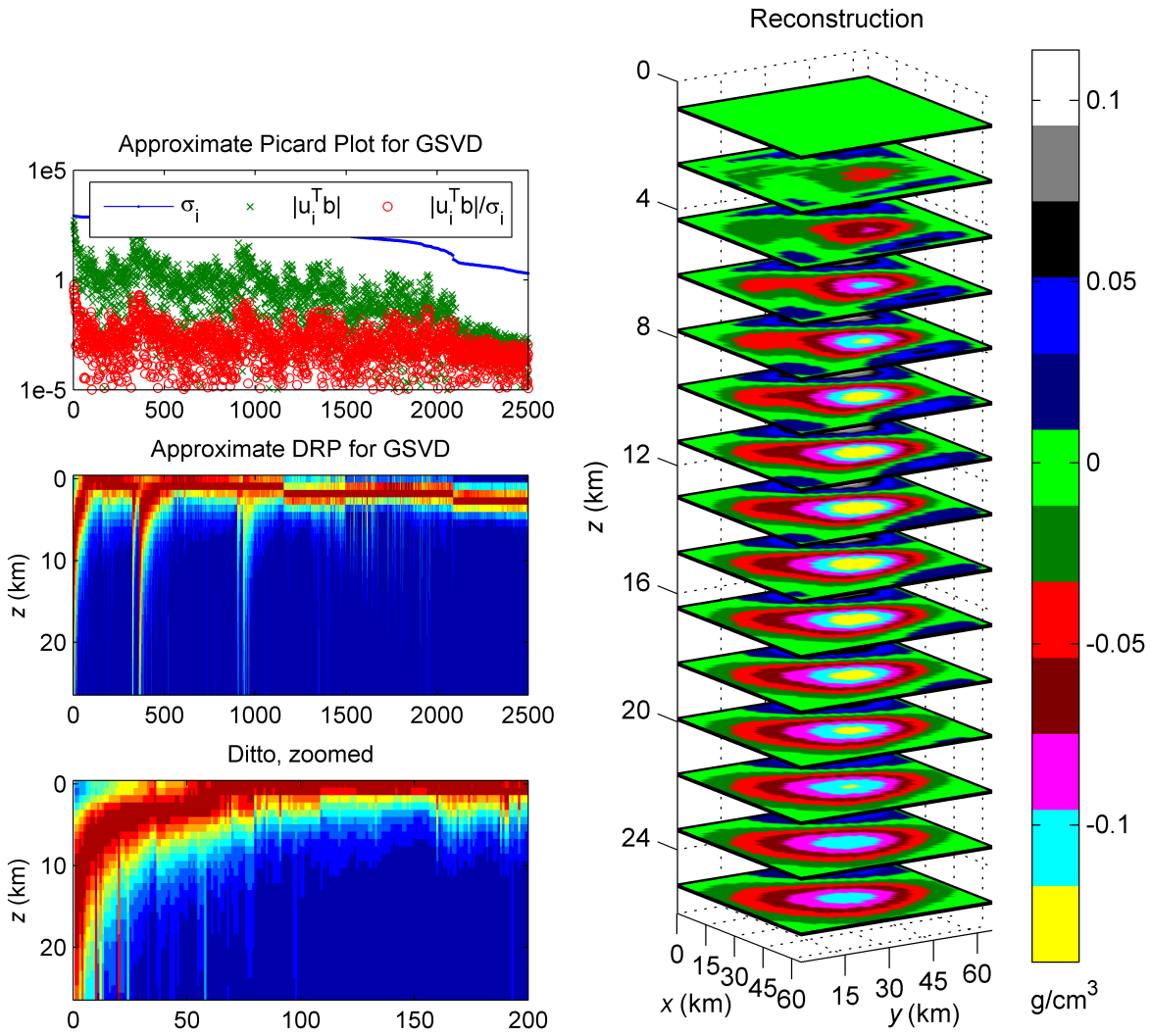

Figure 4.7: Example 4.4. Left: depth resolution analysis of the real data in Fig. 4.6; we used a maximum of $K = 2500$ iterations, and we show both the full APPROXDRP and a zoom on the first 200 components. Right: the CGLS reconstruction using only $k = 200$ iterations. Note the different color map used here to emphasize the depth range of the portion of the structure with the lowest density contrast ($-0.15\,\mathrm{g/cm^3}$).

presence of a low-density zone located between about 8 km and 20 km b.s.l. and characterized by a density contrast of about $-0.15\,\mathrm{g/cm^3}$. This structure extends southwestward and is mostly confined inside the Campanian Plain.

The value of the density contrast found in this analysis is compatible with the presence of trachybasaltic magma in crystalline host rocks, and it is similar to that found by Rapolla et al. [29]. The location and dimensions of the reconstructed structure are consistent with the results of the above cited seismic studies and with the hypothesis that it could be the magmatic reservoir feeding the eruptive centers of the whole Campanian volcanic region.

Conclusion

As a computationally favorable alternative to the SVD-based Depth Resolution Plot, DRP, [11] we introduced the approximate DRP, ApproxDRP, which is based on approximations of the singular vectors obtained by the iterative Lanczos bidiagonalization algorithm. Similar to the DRP, ApproxDRP allows an analysis of how the depth resolution in potential-field inversion is influenced by the regularization and the noise – and since it is based on an iterative method it is well suited for large-scale problems. We also showed that the use of the Lanczos bidiagonalization algorithm leads to CGLS reconstructions that are regularized solutions comparable, e.g., with those computed by means of the SVD. When used for large-scale problems whose dimensions make the use SVD impractical or not feasible, the ApproxDRP allows a reliable analysis of the retrievable depth information, and it effectively guides the user in choosing the optimal number of iterations, for a given problem. The power of the proposed analysis method was shown by its application to real data measured in the Campanian Plain, Neapolitan volcanic area.

Bibliography

[1] AGIP – Agenzia Generale Italiana Petroli, 1987. Geologia e geofisica del sistema geotermico dei Campi Flegrei. Servizi Centrali per l'Esplorazione, SERG-MMERG, San Donato Milanese (in Italian).

[2] Aster, R. C., Borchers, B. & Thurber, D. J., 2005. *Parameter Estimation and Inverse Problems*, Elsevier Academic Press, Amsterdam, the Netherlands.

[3] Auger, E., Gasparini, P., Virieux, J. & Zollo, A., 2001. Seismic evidence of an extended magmatic sill under Mt. Vesuvius. *Science*, **294**, 1510–1512.

[4] Björck, Å., 1996. *Numerical Methods for Least Squares Problems*, SIAM, Pa.

[5] Blakely, R. J., 1996. *Potential theory in gravity and magnetic applications*, Cambridge University Press.

[6] Cassano, E. & La Torre, P., 1987. Geophysics. In Rosi, M. & Sbrana, A. (Eds.), *Phlegrean Fields: Consiglio Nazionale delle Ricerche (CNR)*, Quaderni della Ricerca Scientifica, 103–133.

[7] Cella, F. & Fedi, M., 2012. Inversion of potential field data using the structural index as weighting function rate decay. *Geophysical Prospecting*, **60**, 313–336.

[8] Chung, J., Knepper, S. & Nagy, J. G., 2011. Large-scale inverse problems in imaging. In Scherzer, O. (Ed.), *Handbook of Mathematical Methods in Imaging*, Springer, pp. 43–86.

[9] Di Stefano, R., I. Bianchi, M. G. Ciaccio, G. Carrara, and E. Kissling, 2011. Three-dimensional Moho topography in Italy: new constraints from receiver functions and controlled source seismology, *Geochem. Geophys. Geosyst.*, **12**, Q09006, DOI 10.1029/2011GC003649.

[10] Engl, H. W., Hanke, M. & Neubauer, A., 1996. *Regularization of Inverse Problems*, Kluwer, Dordrecht.

[11] Fedi, M., Hansen, P. C. & Paoletti, V., 2005. Tutorial: Analysis of depth resolution in potential-field inversion. *Geophysics*, **70**, A1–A11.

[12] Fedi, M., Hansen, P. C. & Paoletti, V., 2007. Ambiguity and depth resolution in potential field inversion. *Comm. SIMAI Congress*, **2**. Open access: http://cab.unime.it/journals/index.php/congress/article/view/159/159.

[13] Fedi, M. & Rapolla, A., 1999. 3-D inversion of gravity and magnetic data with depth resolution. *Geophysics*, **64**, 452–460.

[14] Hansen, P. C., 2010. *Discrete Inverse Problems – Insight and Algorithms*, SIAM, Pa.

[15] Hansen, P. C., Sørensen, H. O., Sükösd, Z. & Poulsen, H. F., 2009. Reconstruction of single-grain orientation distribution functions for crystalline materials. *SIAM J. Imaging Sci.*, **2**, 593–613.

[16] Lelièvre, P. G. & Oldenburg, D. W., 2009. A comprehensive study of including structural orientation information in geophysical inversions, *Geophysical Journal International*, **178**, 623–637.

[17] Li, Y. & Oldenburg, D. W., 1996. 3-D inversion of magnetic data, *Geophysics*, **61**, 394–408.

[18] Li, Y. & Oldenburg, D. W., 1998. 3-D inversion of gravity data, *Geophysics*, **63**, 109–119.

[19] Manne, R., 1987, Analysis of two partial-least-squares algorithms for multivariate calibration, *Chemometrics and Inteligent Laboratory Systems*, **2**, 187–197 (Proceedings of the Multivariate Statistical Workshop for Geologists and Geochemists, Ulvik, Hardanger, Norway, 2-5 June 1986, ed. Kvalheim, O. M.). *Proceedings of the Multivariate Statistical Workshop for Geologists and Geochemists*, pp. 187–197.

[20] Menke, W., 2012. *Geophysical Data Analysis: Discrete Inverse Theory*, 3rd Edition, Academic Press, Oxford, UK.

[21] Paige, C. C. & Saunders, M. A., 1982. LSQR: an algorithm for sparse linear equations and sparse least squares, *Trans. on Math. Software*, **8**, 43–71.

[22] Paoletti V., D'Antonio M., Rapolla A., 2013. The structural setting of the Ischia Island within the Neapolitan solcanic area: inferences from geophysics and geochemistry, *Journal of Volcanology and Geothermal Research*, **249**, 155–173. DOI 10.1016/j.jvolgeores.2012.10.002.

[23] Paoletti V., Fedi M., Florio G., Supper R., Rapolla A., 2004. The new integrated aeromagnetic map of the Phlegrean Fields Volcano and surrounding areas, *Annals of Geophysics*, **47**, 1569–1580.

[24] Paoletti, V., Ialongo, S., Florio, G., Fedi, M. & Cella, F., 2013. Self-constrained inversion of potential fields, *Geophysical Journal International*, **195**, 854–869, DOI 10.1093/gji/ggt313.

[25] Paoletti V., Secomandi M., Florio G., Fedi M., Rapolla A., 2005. The integration of remote sensing magnetic data in the Neapolitan volcanic district, *Geosphere*, **1**, 85–96.

[26] Pilkington, M., 2009. 3D magnetic data-space inversion with sparseness constraints, *Geophysics*, **74**, L7–L15.

[27] Pilkington, M., 2012. Analysis of gravity gradiometer inverse problems using optimal design measures, *Geophysics*, **77**, G25–G31.

[28] Portniaguine, O. & Zhdanov M. S., 2002. 3-D magnetic inversion with data compression and image focusing, *Geophysics*, **67**, 1532–1541.

[29] Rapolla, A., Fedi, M. & Fiume, G., 1989. Crustal structure of the Ischia-Phlegrean Fields geothermal area, near Naples (Italy), from gravity and aeromagnetic data. *Geophysical Journal*, **97**, 409–419.

[30] Sartori, R., 2003. The Tyrrhenian back-arc basin and subduction of the Ionian lithosphere. *Episodes*, **26**, 217–221.

[31] Silva, J. B. C. & Barbosa, V. C. F., 2006. Interactive gravity inversion, *Geophysics*, **71**, J1–J9. DOI 10.1190/1.2168010.

[32] Wold, H., 1966. Estimation of principal components and related models by iterative least squares. In Krishnaiaah, P. R. (Ed.), *Multivariate Analysis*, Academic Press, 391–420.

[33] Zhdanov, M. S., 2002. *Geophysical inverse theory and regularization problems*, Elsevier Science Publishing Co.

[34] Zollo, A., Gasparini, P., Virieux, J., le Meur, H., de Natale, G., Biella, G., Boschi, E., Capuano, P., de Franco, R., dell'Aversana, P., de Matteis, R., Guerra, I., Iannaccone, G., Mirabile, L. & Vilardo, G., 1996. Seismic evidence for a low-velocity zone in the upper crust beneath Mount Vesuvius. *Science*, **274**, 592–594.

[35] Zollo, A., Maercklin, N., Vassallo, M., Dello Iacono, D., Virieux, J. & Gasparini, P, 2008. Seismic reflections reveal a massive melt layer feeding Campi Flegrei caldera. *Geophysical Research Letters*, **35**, L12306.